

See discussions, stats, and author profiles for this publication at: <https://www.researchgate.net/publication/230565761>

Multiscale Charge Injection and Transport Properties in Self-Assembled Monolayers of Biphenyl Thiols with Varying Torsion Angles

ARTICLE *in* CHEMISTRY - A EUROPEAN JOURNAL · AUGUST 2012

Impact Factor: 5.73 · DOI: 10.1002/chem.201201858 · Source: PubMed

CITATIONS

19

READS

48

9 AUTHORS, INCLUDING:



Núria Crivillers

Spanish National Research Council

38 PUBLICATIONS 767 CITATIONS

SEE PROFILE



Emanuele Orgiu

University of Strasbourg

62 PUBLICATIONS 663 CITATIONS

SEE PROFILE



Ramakrishnappa Thippeswamy

Dayananda Sagar University

39 PUBLICATIONS 137 CITATIONS

SEE PROFILE



Paolo Samorì

University of Strasbourg

275 PUBLICATIONS 7,413 CITATIONS

SEE PROFILE

Multiscale Charge Injection and Transport Properties in Self-Assembled Monolayers of Biphenyl Thiols with Varying Torsion Angles

Appan Merari Masillamani,^[a] Núria Crivillers,^[a] Emanuele Orgiu,^[a] Jürgen Rotzler,^[b] David Bossert,^[b] Ramakrishnappa Thippeswamy,^[d] Michael Zharnikov,^{*,[d]} Marcel Mayor,^{*,[b, c]} and Paolo Samorì^{*,[a]}

Abstract: This article describes the molecular structure–function relationship for a series of biphenylthiol derivatives with varying torsional degree of freedom in their molecular backbone when self-assembled on gold electrodes. These biphenylthiol molecules chemisorbed on Au exhibit different tilt angles with respect to the surface normal and different packing densities. The charge transport through the biphenylthiol self-assembled monolayers (SAMs) showed a characteristic decay

trend with the effective monolayer thickness. Based on parallel pathways model the tunneling decay factor β was estimated to be 0.27 \AA^{-1} . The hole mobility of poly(3-hexylthiophene)-based thin-film transistors incorporating a biphenylthiol SAM coating the Au

Keywords: biphenylthiols • charge tunneling • hole injection barrier • molecular electronics • self-assembly

source and drain electrodes revealed a dependence on the injection barrier with the highest occupied molecular orbital (HOMO) level of the semiconductor. The possible role of the resistivity of the SAMs on transistor electrodes on the threshold voltage shift is discussed. The control over the chemical structure, electronic properties, and packing order of the SAMs provides a versatile platform to regulate the charge injection in organic electronic devices.

Introduction

The prediction by Aviram and Ratner that organic molecules could exhibit an electrical-current rectification property^[1] triggered remarkable research efforts, which have been blooming with the emergence of molecular electronics. The nanoscale electronic properties in molecule-based junctions can be controlled through a proper molecular design.^[2] A particular approach for molecular-junction preparation is the chemisorption of sulfur-exposing molecules on metallic surfaces like Au, Ag and Pt, which provides a facile route to

form highly ordered self-assembled monolayers (SAMs).^[3] These junctions can feature distinct functionalities including electrical-current rectification,^[2c,4] photo-responsive current switching,^[2b,5] wettability, and work function modification.^[6] These tunable properties, which depend on the choice of the molecule and metal electrode, have been shown to make SAMs ideal components for optimizing the charge injection at metal–organic interfaces for application in organic thin-film transistors (OTFTs). A thorough knowledge on the transport properties through the SAMs is therefore important for the design and further fabrication of the organic electronic devices incorporating these monolayers. The charge transport through molecules sandwiched between two metallic electrodes has been probed by using a variety of different techniques, such as conducting-probe atomic force microscopy (CP-AFM),^[2b,8] Hg-droplet-based electrodes,^[9] mechanically controlled break junctions,^[10] scanning tunneling microscopy (STM),^[2a,11] nanopores,^[12] crossed-wire tunneling junctions,^[13] junctions formed by surface-diffusion-mediated deposition (SDMD),^[14] and non-intrusive conformational junctions on the SAM with an eutectic alloy of liquid-metallic gallium–indium (GaIn^E) tip as the probe electrode.^[15] Each of the above-mentioned techniques has its own pros and cons, with a variable range of set-up complexities, junction areas, geometry of contacts, and conditions necessary for experimentation. The GaIn^E -based junction is particularly interesting, since it exploits the peculiar property of liquid-metallic gallium–indium to behave like a non-Newtonian liquid at room temperature. Importantly, it can be molded into a conical tip that retains its shape under am-

[a] A. M. Masillamani, Dr. N. Crivillers, Dr. E. Orgiu, Prof. P. Samorì
ISIS & icFRC, Université de Strasbourg & CNRS
8 allée Gaspard Monge, 67000 Strasbourg (France)
E-mail: samori@unistra.fr

[b] J. Rotzler, D. Bossert, Prof. M. Mayor
Department of Chemistry, University of Basel
St. Johannisring 19, 4056 Basel (Switzerland)
E-mail: marcel.mayor@unibas.ch

[c] Prof. M. Mayor
Karlsruhe Institute of Technology (KIT)
Institute for Nanotechnology
P.O. Box 3640, 76021 Karlsruhe (Germany)

[d] Dr. R. Thippeswamy, Prof. M. Zharnikov
Angewandte Physikalische Chemie, Universität Heidelberg
Im Neuenheimer Feld 253, 69120 Heidelberg (Germany)
E-mail: Michael.Zharnikov@urz.uni-heidelberg.de

Supporting information for this article is available on the WWW under <http://dx.doi.org/10.1002/chem.201201858>.

bient conditions. Significantly, GaIn^E features an intrinsic property to form a thin oxide layer (ca. 1–2 nm) when exposed to air; importantly, such a self-bonding oxide (Ga₂O₃) sheath enables the bulk of the underlying GaIn^E to hold its shape.^[15] The ease of forming reliable and reproducible conical-shaped GaIn^E tips has been exploited to study the charge transport of delicate μm^2 -sized single-molecule-layer junctions.^[2c,15,16]

In contrast, other types of counter electrodes, like those based on a Hg drop, needed a protecting alkanethiol layer coating the counter electrode to improve the yield^[17] by mitigating formation of junction short-circuits when placing the drop in contact with the SAM on the metallic substrate.^[9b,18] Similarly, a thin conducting film of poly(3,4-ethylenedioxythiophene)–poly(styrenesulfonate) (PEDOT:PSS) polymer^[5c,19] or graphene^[20] has been employed to protect the SAM prior to deposition of top Au electrodes in large-area molecular junctions.

Traditionally *n*-alkanethiols have been widely studied,^[8a,9b,11,12,16c,19,21] and successfully employed to change the wettability and work function properties of gold contacts, but their scope as functional components for molecular electronic devices is limited. The better conducting aromatic compounds offer a far more versatile platform to modulate their electronic properties by altering the chemical structure of the molecule^[16a,22] or by influence of external stimuli like thermal energy or light.^[2b,16b,18b]

Here we have designed and synthesized a new library of monothiolated biphenyl molecules featuring different torsion angles between the two phenyl subunits along the molecular backbone. Although there have been studies on the single-molecular conductance of biphenyl units thiolated in both α and ω positions,^[2a,23] the charge transport through biphenyl monothiol SAMs with varying torsion in the long molecular axis have not yet been explored on a macroscopic scale. On the one hand, once chemisorbed on Au(111), we investigated the charge transport through the monothiol biphenyl SAMs embedded in a two-terminal junction based on a top GaIn^E counter electrode. On the other hand, we functionalized the source and drain electrodes of OTFTs with monothiol biphenyl SAMs and exploited them to tune the charge injection at the metal–organic interface of the devices.

The torsion angle between individual aromatic rings in doubly thiolated biphenyl derivatives has been shown, in a single-molecule break junction based on STM, to govern the electrical conductivity across the single-molecule scale.^[2a,23] Both theoretical^[22c] and experimental results^[2a,23,24] provided evidence for a correlation between the cosine square of the torsion angle and the single-molecule conductance. The increasing torsion angle is accompanied by a decrease in the extent of the geometrical overlap of p_z orbitals; as a result the corresponding single-molecule conductance decreases, since the electron-transfer rate changes as a function of the square of p_z orbital overlap. Moreover if the contribution due to tunneling transport through the σ orbitals is neglected, the theory predicts a linear relationship

between the molecular conductance with the square of the cosine of the torsion angle.^[25]

The different mono-thiolated biphenyl derivatives designed, synthesized and exploited in the present study are 1) 9*H*-fluorene-2-thiol, denoted here as **5mBPT** due to the fluorene group bridging the two individual phenyl rings; 2) 1,2-bis(9,10-dihydrophenanthren-2-yl)disulfane denoted as **6mBPT**; 3) (1,1'-biphenyl)-4-thiol denoted as **BPT**; and 4) 2,2'-dimethyl(1,1'-biphenyl)-4-thiol denoted as **tBPT** (i.e., twisted **BPT**).

Experimental Section

Thiol solution preparation: 1 mM solutions in CHCl₃ were prepared and stored in an inert N₂ filled atmosphere of a glove box (Jacomex).

SAM fabrication procedure: For X-ray spectroscopy and charge-transport measurements with a GaIn^E setup, the SAMs were prepared on commercial gold(111) evaporated on mica substrates (Georg Albert PVD, Germany) with an Au thickness of 300 nm. The substrates were immersed and incubated in the corresponding 1 mM biphenylthiol solution under an N₂ atmosphere for 24 h to obtain the desired monolayers. For work function and contact-angle experiments, Au with a thickness of 50 nm was evaporated onto glass slides with an adhesion Cr layer of 10 nm at a base pressure of about 10^{−6} mbar in a Plassys MEB 300 thermal evaporator and then immediately immersed in the respective thiol solution for 24 h under inert conditions inside a glovebox. For all the experiments, once removed from the thiol solution, the substrates were rinsed with copious amounts of CHCl₃ in ambient conditions. All the substrates were treated with UV/Ozone prior to immersion in the respective thiol solutions for SAM formation.

X-ray spectroscopy measurements: The structural characterization of the SAMs was performed by means of synchrotron-based high-resolution X-ray photoelectron spectroscopy (HRXPS) and angle-resolved near-edge X-ray absorption fine structure (NEXAFS) spectroscopy. The HRXPS and NEXAFS spectroscopy experiments were performed at the bending magnet HE-SGM beamline at the synchrotron storage ring BESSY II in Berlin (Germany). The measurements were carried out under room temperature and ultra-high vacuum (UHV) conditions with a base pressure of at least 1.5 × 10^{−9} mbar or higher. The time for spectral acquisition was carefully selected such that no noticeable sample damage by the primary X-rays was observed during the measurements.^[26] The spectra were recorded in normal emission geometry. C 1s, S 2p, and Au 4f HRXPS spectra were acquired at photon energies (PEs) of 350 and 580 eV. The O 1s spectral range was monitored and the binding energy (BE) scale was referenced to the position of the Au 4f_{7/2} emission line of an Au substrate with a SAM of dodecanethiol at an energy of 83.95 eV, which is given by the latest ISO standard.^[27] The energy resolution was approximately 0.3 eV at a PE of 350 eV. The resulting HRXPS spectra was fitted by symmetric Voigt functions of either a Shirley-type or linear background; the fits were performed self-consistently (i.e., the same peak parameters were used in identical regions of the spectrum), which resulted in the spectrum accuracy for the BE at FWHM values in the range of 0.05 eV. In the case of the S 2p_{3/2,1/2} doublets, we used a pair of peaks with the same FWHM, a branching ratio of 2 (2p_{3/2}/2p_{1/2}), and a spin-orbit splitting verified by the fit of about 1.18 eV.^[28]

The NEXAFS spectra were acquired at C K-edge in partial electron yield mode with a retarding voltage of −150 V and linearly polarized light with a polarization factor of about 91 %. To gather details of the orientational order of the SAMs the angle of the incident light was varied from 90 to 20° in steps of 10–20°, which corresponds to progression of the *E* vector from the surface normal to the plane close to the sample surface.^[29] The energy resolution of the spectra was about 0.3 eV. The raw NEXAFS spectrum of each sample was normalized by dividing by the incident photon flux for a clean gold reference sample^[30] and the

energy scale was gauged to the most pronounced π^* resonance of highly oriented pyrolytic graphite at 285.38 eV.^[31]

Charge transport in SAMs: To estimate the rate of charge transport through the SAMs on Au a two terminal setup composed of a liquid-metallic alloy GaIn^E was employed as the top-probe electrode. An airtight digital syringe held an adequate reservoir of GaIn^E, which could be manipulated to dispense the liquid metal in a controlled fashion, and was then molded to a conical shaped tip (see Figure S5 Supporting Information). The junction, comprising the SAM sandwiched between Au and GaIn^E, could be formed very accurately by means of a servo-controlled xyz stage through careful approach of the GaIn^E tip. This was accomplished by raising the stage supporting the functionalized substrate to gently contact the apex of the hanging GaIn^E tip (monitored in real-time by using a CCD camera). To ensure a greater control during approach in the z-axis direction (vertical) and higher versatility of movement in the x-y axes direction (lateral), we kept the position of the syringe holding the GaIn^E tip fixed, thereby only moving the stage supporting the sample. The necessary potentials across the junctions were provided by an external supply unit (Keithley 2635 SMU, Keithley instruments Inc) interfaced through a triaxial cable to minimize signal losses. In particular, a DC bias was applied to the GaIn^E tip, while holding the Au electrode in electrical ground. Current versus potential (I - V) traces were recorded by applying potential sweep across the junction from $-0.5 \rightarrow +0.5$ V (unidirectional trace), starting from -0.5 V proceeding to $+0.5$ V and ending at -0.5 V for the case of a bidirectional trace (see Supporting Information) in 20 mV steps. The measured I values were translated into a corresponding current density (J) by normalizing to the junction contact area. The area in contact with the GaIn^E tip was estimated from the image captured by using a USB camera and calibrating that to a sample of known thickness. The procedure for contact area estimation was performed with the following steps. A cross-sectional side view image of a substrate with standard thickness (IPMS Fraunhofer) was captured and the corresponding number in pixels was estimated for this thickness. From this the distance value for an individual pixel was extracted, as a way to calibrate our optical system. Images were captured for each junction formed and then the total number of pixels was estimated in the region of tip contact by using ImageJ 1.42q (an open source software). The number of pixels was then re-translated into distance in μm , corresponding to the diameter for the junctions when the GaIn^E tip established contact with the SAM. This diameter was then used to estimate the contact area by using a standard formula for the area of a circle. It has previously been shown that the actual area of the GaIn^E tip in contact with an ITO surface is roughly 25% of the actual area,^[4] this is probably due to the formation of micromenisci^[32] at the sides of the liquid-metallic GaIn^E tip apex. Hence to arrive at an accurate consensus of the current density for a given applied bias in the sweep voltage range, we measured a large number of I - V traces, in “ n ” junctions.

Electrode wettability tests: The aqueous contact angle at the SAM-ambient interface was measured by means of a Krüss DSA 100 goniometer. The contact angle and the derived work of adhesion provided qualitative information on the surface wettability of electrodes incorporated in OTFTs.

Work function measurements: The work function of the modified Au substrates was measured by means of macroscopic Kelvin probe (Kelvin Probe Technology Ltd). The contact potential difference method, using a commercial Au reference tip was employed to record the work function of the Au and Au-SAM surface.

OTFTs fabrication and electrical characterization: $1.5 \times 1.5 \text{ cm}^2$ Si/SiO₂ substrates (IPMS Fraunhofer) composed of thermally grown SiO₂ layer on n^{++} Si, serving as the gate electrode, and pre-patterned Au electrodes

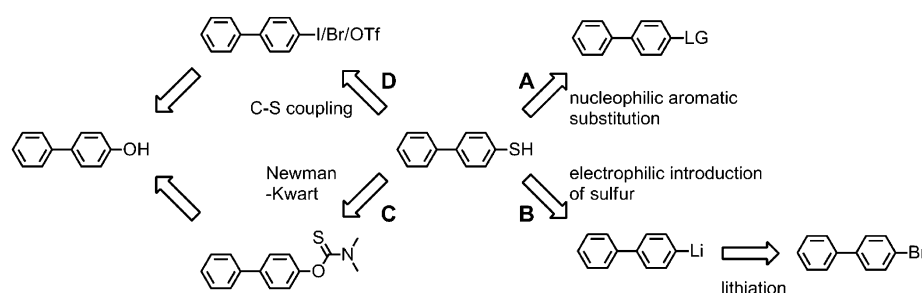
deposited on the SiO₂ layer, serving as source-drain electrodes, were used to fabricate the thin-film transistor. The channel length (L) and width (W) for the TFTs that were characterized amounted to 10 and 10000 μm , respectively. To complete the OTFT device a poly(3-hexylthiophene) (P3HT) solution (120 μL of 2 mg mL^{-1} in toluene) was spin-coated on the substrates. After spin-coating of P3HT, the solvent was allowed to evaporate for about 48 h prior to electrical characterization. This characterization was performed by means of a dual channel source meter (Keithley 2636 A SMU) in the dark. Triaxial cables were employed to minimize signal losses. The complete fabrication and electrical characterization were performed inside a N₂-filled glovebox (Jacomex) with O₂ levels < 10 ppm, with the exception of the rinsing step after SAM formation to remove physisorbed material on the electrodes, which was performed in ambient conditions.

Morphological characterization: The morphology of the semiconductor film on the Au electrodes of the OTFT device configuration was mapped by atomic force microscopy (AFM) from Digital Instruments Dimension 3100 (Bruker Instruments Inc, USA) operating in the intermittent contact mode.

Ionization energy of P3HT: The ionization energy of a drop-casted P3HT film was recorded by ambient ultraviolet photoelectron spectroscopy by using a Riken AC2 spectrophotometer. An estimate of the ionization energy was attained from relation of square root of the photoelectron yield for the incident PE.

Results

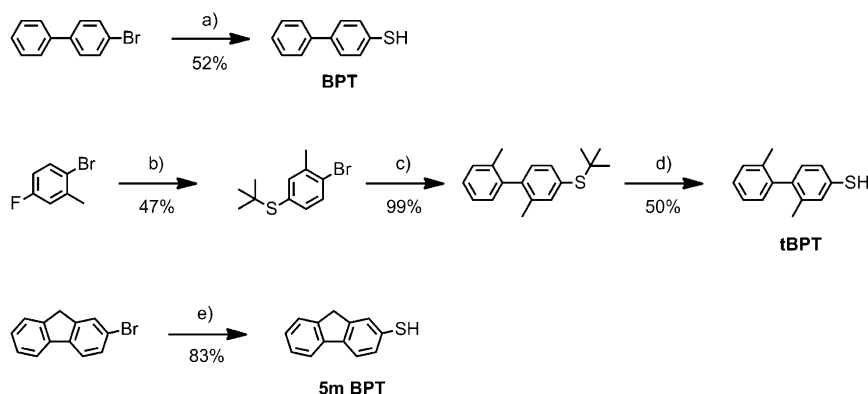
Synthesis: Several different strategies can be envisaged to introduce a thiol moiety on aromatic systems. The maybe most straightforward ones are displayed in Scheme 1. Nucleophilic aromatic substitution of aryl halides with a strong



Scheme 1. Retrosynthetic strategies to introduce the sulfur moiety to a biphenyl core.

nucleophilic thiol is a valuable method if the resulting thiophenol has to be obtained in a protected form (method A). A second strategy can be the introduction of the thiol by reacting a lithiated aryl with sulfur, forming the sulfide, followed by trapping with a protection group or protonation (method B). Method C can be an alternative strategy if the syntheses of aryl halide precursors are troublesome, for example, because of low selectivity. The precursor for the final Newman-Kwart rearrangement is a phenol for which a variety of different synthetic routes are known. Furthermore the polarity of the phenol often improves the purification and isolation procedures. A major disadvantage of method C is the increased number of synthetic transformations. The monomethoxy biphenyl can also be converted to the thiol by C-S hetero-cross-coupling protocols (method D).

(1,1'-Biphenyl)-4-thiol (**BPT**) was synthesized according to synthetic method **B**. The commercially available 4-bromobiphenyl was treated with *tert*-butyl lithium at -78°C for 1 h. Then ground elemental sulfur was added to the lithiated biphenyl in small portions. The final target compound **BPT** was obtained after quenching of the sulfide with hydrochloric acid and purification by basic extraction followed by sublimation in 52% (Scheme 2 top).



Scheme 2. Synthesis of 4-thiobiphenyls with varying torsion angles (**BPT**, **tBPT**, and **5mBPT**). a) 1.) *t*BuLi, THF, -78°C , 1 h, then RT, 2.) S_8 , RT, 3 h, 3.) aq. HCl, RT, 30 min; b) sodium 2-methylpropane-2-thiolate, DMF, reflux 2 h; c) *o*-tolylboronic acid, $[\text{Pd}(\text{PPh}_3)_4]$, Cs_2CO_3 , toluene/EtOH 2:1, 95°C , 24 h; d) BBr_3 (1 M in dichloromethane), 0°C , 2.5 h, then MeOH; e) sodium thiomethoxide, DMI, 120°C , 18 h, then aq. HCl.

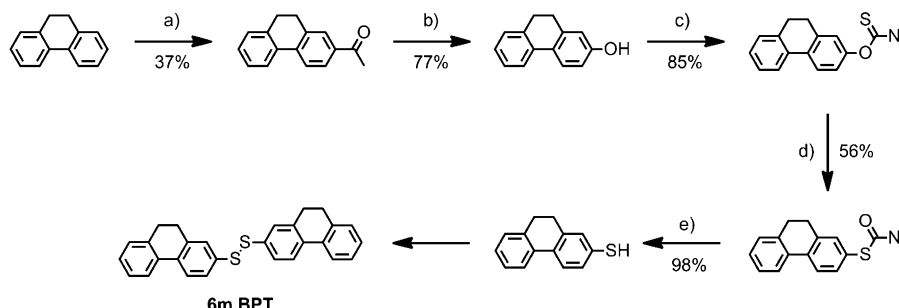
2,2'-Dimethyl(1,1'-biphenyl)-4-thiol (**tBPT**) was synthesized in a three-step sequence starting from 1-bromo-4-fluoro-2-methylbenzene (Scheme 2, middle). The thiol moiety was introduced at the first step of the synthesis, since nucleophilic substitution of 2,2'-dimethyl-4-fluorobiphenyl with sodium *tert*-butylthiolate was not successful. Fluorobenzene was transformed to (4-bromo-3-methylphenyl)-*tert*-butylsulfane by a nucleophilic aromatic substitution using sodium *tert*-butylthiolate as a nucleophile. Subsequent Suzuki cross-coupling with *o*-tolylboronic acid by using tetrakis(triphenylphosphine)palladium as a catalyst and cesium carbonate as a base in a solvent mixture of toluene/EtOH 2:1 afforded the *tert*-butyl-protected biphenylthiol. Deprotection by boron tribromide yielded after quenching with methanol the desired target compound **tBPT** in 23% yield over three steps. Biphenylthiol **tBPT** was further purified by Kugelrohr distillation.

For the synthesis of the fluorene derivative (**5mBPT**) method **A** was used (Scheme 2 bottom). In contrast to the synthesis of **BPT**, the presence of a strong base readily leads to deprotonation of the bridging

methylene protons, due to the increased acidity of this doubly stabilized benzylic position. To prevent side product formation, commercially available 2-bromo-9*H*-fluorene was treated with sodium thiomethoxide in 1,3-dimethylimidazolidinone (DMI) at 120°C . Nucleophilic aromatic substitution yields the methyl-protected thiophenol, which was deprotected in situ by the excess of sodium thiomethoxide. After quenching with hydrochloric acid, basic extraction afforded target compound **5mBPT** in high purity (83%).

The 1,2-bis(9,10-dihydrophenanthren-2-yl)disulfane (**6mBPT**) was synthesized by use of a Newman-Kwart rearrangement of 9,10-dihydrophenanthren-2-ol.^[61] Attempts to monobrominate 9,10-dihydrophenanthrene at the 4-position were not successful. Even though the formation of the desired starting material was observed by ^1H NMR spectroscopy, it was impossible to isolate 2-bromo-9,10-dihydrophenanthrene from the crude, due to the lack of polarity of all formed compounds. To avoid the difficulties in regioselectivity and isolation, in a first step

9,10-dihydrophenanthrene was acetylated in the 2-position by using a Friedel-Crafts acylation protocol^[5c] in 37% yield. A sequence of Baeyer-Villiger oxidation followed by ester cleavage afforded 9,10-dihydrophenanthren-2-ol in 77% over both steps (Scheme 3). The *O*-thiocarbamate necessary for the envisaged Newman-Kwart rearrangement was then synthesized by reacting the dihydrophenanthrene-2-ol with dimethylcarbamoyl chloride and sodium hydride as a base. The thermally activated Newman-Kwart rearrangement, in which an *O*-thiocarbamate rearranges to a *S*-thiocarbamate, was carried out at 260°C in diphenyl ether. After successful rearrangement the solvent was removed by column chroma-



Scheme 3. Synthesis of 1,2-bis(9,10-dihydrophenanthren-2-yl)disulfane (**6mBPT**). a) Acetyl chloride, AlCl_3 , dichloromethane, 0°C , 1 h, then RT, 2 h; b) 1.) *m*-CPBA, dichloromethane, 0°C , 3 h, then RT, 95 h, 2.) conc. aq. HCl, MeOH, RT, 18 h; c) dimethylcarbamoyl chloride, NaH, DMF, 80°C , 2 h, then RT, 15 h; d) Ph_2O , 260°C , 2 h; e) KOH, MeOH, 80°C , 3 h.

tography and the obtained *S*-thiocarbamate cleaved in strong basic medium to yield the free thiol **6mBPT** in 98% yield. The free thiol was not stable towards formation of disulfides even when stored at -18°C under argon atmosphere.

All desired compounds were further purified by vacuum sublimation (solids) or Kugelrohr distillation prior to the physical chemical investigations. The target compounds were characterized by NMR spectroscopy, mass spectrometry, GC-MS, and elemental analysis. The purity of **tBPT** after storage over two months under argon atmosphere at 0°C was confirmed by GC-MS.

Structural characterization of the SAMs: The structural analysis on the surface of the Au(111) with the different biphenylthiol SAMs chemisorbed on its surface was performed by means of HRXPS complemented by NEXAFS spectroscopy to cast light onto the electronic structure and tilt angle of the adsorbed molecular layers.

HRXPS on biphenylthiol SAMs: The C 1s and S 2p HRXPS spectra of all the SAMs used in this study are shown in Figure 1. The spectra were gathered at wave energies of 350 and 580 eV for the C 1s and at 350 eV for the S 2p emis-

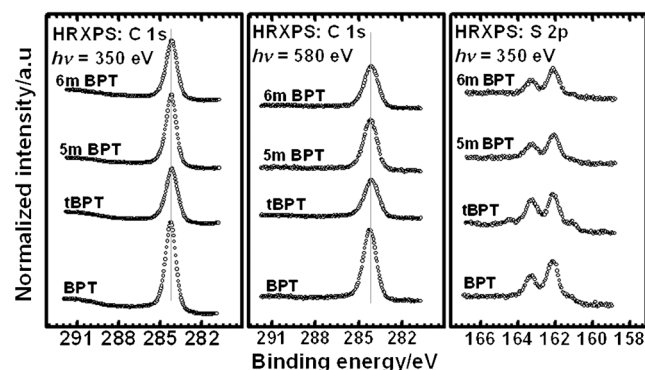


Figure 1. C 1s (left and middle panels) and S 2p (right panel) HRXPS spectra of the target SAMs acquired at photon energies of 350 eV (left and right panels) and 580 eV (middle panel). The gray lines are guide for the eye and are placed at a BE of 284.2 eV.

sion. In the C 1s spectra a single emission at 284.2–284.3 eV is observed, which is attributed to the aromatic backbone of the SAM constituents. A characteristic emission in a similar binding energy (BE) range of 284.2–284.3 eV has previously been reported for biphenyl-substituted dithiols (BPDTS).^[33] The S 2p spectra of the SAMs are dominated by the S $2p_{3/2,1/2}$ doublet at 162.0 eV (S $2p_{3/2}$), corresponding to a thiolate-type bonding of the SAM constituents to the substrate.^[33,34] This doublet is the only feature in the spectra of **6mBPT** and **5mBPT** SAMs, but is accompanied by an additional weak doublet at a BE of about 161.0 eV (S $2p_{3/2}$) in the spectra of **BPT** and **tBPT** monolayers and by a further weak doublet at a BE of 163.4–163.5 eV in the spectrum of **tBPT** SAMs. The former doublet can be assigned to the dif-

ferently (but strongly) bound SAM constituents, while the latter to the unbound or weakly bound molecules that are either caught in the hydrocarbon matrix of the SAM or physisorbed at the SAM/ambience interface;^[35] the content of all these species is however quite low. Further, the effective thicknesses of the SAMs were calculated according to standard procedure by using the intensity ratios of the C 1s and the Au 4f signals and the standard attenuation lengths for the Au 4f and C 1s emissions at the given kinetic energies.^[34,36] In addition to the above thickness values, the packing density in the target SAMs were estimated on the basis of the S 2p/Au 4f intensity ratio, using a SAM with a known packing density, namely, dodecanethiol on Au(111) in the given case, as a reference.^[37] The derived values of the effective thickness and packing density of the target SAMs are displayed in Table 1. A smaller value of the thickness of the SAM in comparison to the estimated length of the **BPT** molecule (ca. 12 Å) in the gas phase suggests that the SAM constituents have some degree of inclination. The packing density of the target SAMs exhibits the following trend **BPT** > **6mBPT** > **5mBPT** > **tBPT**.

Table 1. Effective SAM thickness in Å along with packing density of the molecules in for the different **BPT** SAMs in comparison to the reference of dodecanethiol (C12) SAM.

	Effective thickness [Å]	$I(\text{S } 2p)/I(\text{Au } 4f_{7/2})$	Packing density $\times 10^{14}$ [mol cm $^{-2}$]
C12	15		4.63
5mBPT	11.68	0.06867	3.67
6mBPT	9.08	0.068842	3.68
BPT	11.45	0.079533	4.25
tBPT	8.13	0.054446	2.91

NEXAFS measurements: Figure 2 shows the C K-edge NEXAFS spectra of the target SAMs. The spectra in the left-hand panel were acquired at the so-called magic X-ray incidence angle (55°), which leads to spectra that are independent of the molecular orientation, representative of the electronic structure of the unoccupied molecular orbitals.^[29] The curves in the right-hand panel are the differences be-

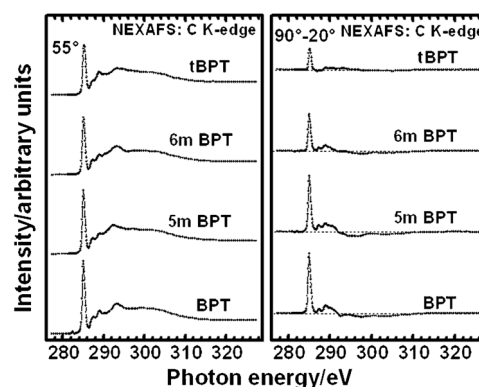


Figure 2. C K-edge NEXAFS spectra of the target SAMs acquired at an incidence angle of 55° (left panel) and the difference of the spectra acquired at X-ray incidence angles of 90° and 20° (right panel). Horizontal dashed lines in the right panel correspond to zero.

tween the spectra acquired at X-ray incidence angles of 90 and 20°; such curves are representative of the molecular orientation.^[29] The spectra are dominated by the intense π_1^* resonance of the phenyl rings at about 285.1 eV accompanied by the respective π_2^* resonance at 288.8 eV, the $R^*/C-S^*$ resonance at about 287.8 eV, and several broad σ^* resonances at higher photon energies (the assignments were performed in accordance with literature data).^[28,30,33,34,38] Note that the pattern of the absorption resonances for the SAMs used in this study is similar to that of benzene, as can be expected.^[36,39] In the case of the **BPT** SAM, this pattern can be attributed to the localization of the excited molecular orbitals at a particular aromatic ring.^[39] In accordance with the literature data,^[33] the aliphatic bridging group in **5m** and **6mBPT** does not change this pattern significantly, which means that the conjugation between the aromatic rings is not affected. Note that this correlates with the spacing between the rings in these compounds, which exceeds a critical value of 1.477 Å.^[40] On the basis of the intensity of the π_1^* resonance, the quality of the target SAMs follows the trend **BPT** > **5mBPT** > **6mBPT** > **tBPT**, in agreement with the HRXPS results (see the previous section). In addition, the π_1^* resonance for the **tBPT** SAMs is somewhat broader than for the other monolayers of this study, which is a further evidence for the higher degree of heterogeneity in this particular film.

In addition to the above analysis of the 55° spectra, information on the molecular orientation in the target SAMs could be obtained on the basis of the entire set of the NEXAFS data. In particular, the average tilt angle of the aromatic chains in these films can be estimated by a quantitative analysis of the angular dependence of the NEXAFS resonance intensities.^[29] For this analysis, the π_1^* resonance was selected as the most intense and distinct resonance in the absorption spectra. In addition, the intensities of this resonance could be derived directly from the NEXAFS spectra, without a sometimes ambiguous fitting procedure. Once these intensities I are known, the average tilt angle α of the π_1^* orbitals with respect to the surface normal can be derived from a standard expression for a vector-type orbital [Eq. (1)],^[29] in which A is a constant, α is the average tilt angle of the molecular orbital, P is the polarization factor and θ is the incidence angle of the incoming X-rays.

$$I(\alpha, \theta) = A \left\{ P \times \frac{1}{3} \left[1 + \frac{1}{2} (3 \cos^2 \theta - 1) (3 \cos^2 \alpha - 1) \right] + (1 - P) \frac{1}{2} \sin^2 \alpha \right\} \quad (1)$$

The tilt angle α of the π_1^* orbitals is directly related to the tilt angle φ of the molecular axis with respect to the surface normal and to the average twist angle ϑ of the aromatic rings with respect to the plane spanned by the surface normal and the molecular axis [Eq. (2)].^[41]

$$\cos \alpha = \cos \vartheta \sin \varphi \quad (2)$$

This expression allows estimation of the tilt angle of the molecular axis as soon as some assumptions about the value of the twist angle are made. In the case of the SAMs of this study it is reasonable to assume a herringbone arrangement, which is typical of aromatic bulk systems and of aromatic SAMs.^[42] This means two different spatial orientations of the aromatic moieties occurring with oppositely signed (i.e., reverse) twist angles $\vartheta_1 = -\vartheta_2$ and the similar tilt angles $\varphi_1 = \varphi_2$. The different signs of the twist angle are not a problem, since $\cos \vartheta$ is an even function. The most reasonable assumption for the absolute value of the twist angle is 32°, which is the value observed in the biphenyl bulk materials^[42a] and well applicable to aromatic SAMs.^[41,43] Table 2 shows the es-

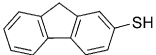
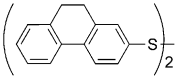
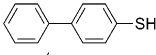
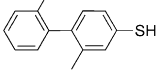
Table 2. Tilt angle and parameters estimated from the NEXAFS data.

	θ_i [°] ^[a]	α [°] ^[b]	ϑ [°] ^[c]	φ [°] ^[d]
5mBPT	0 ^[44]	69.0	32.0	25.0
6mBPT	20 ^[45]	66.9	32.0	27.6
BPT	0 ^[42a]	71.5	32.0	22.0
tBPT	79.7 ^[33]	62.4	32.0	33.0

[a] Solid-state torsion angle. [b] Average tilt angle of π_1^* molecular orbital. [c] Assumed twist angle. [d] Average tilt angle all in degrees.

timated average tilt angles of π_1^* orbitals (α), the tilt angles of molecules (φ), and the assumed twist angle (ϑ). Note that we assume a coplanar arrangement of individual rings within the biphenyl backbone in the **BPT** SAMs, which is a reasonable assumption considering that this arrangement is typical for densely-packed aromatic compounds in which the dihedral rotation is lifted due to the intermolecular interaction.^[42a] The backbone of **5mBPT** SAMs has a planar conformation,^[44] while the torsion angle for the backbone of the **6mBPT** SAM is about 16.8° (see Table 3 and reference [45]). The torsion angle for the backbone of the **tBPT** SAM is close to 80° (see Table 3 and reference [33]), so that the assumed twist angle can only be considered as an average value over the both rings. The accuracy of the derived tilt angles is about $\pm 3^\circ$, which is partly related to the uncertainty of the twist angles. The derived tilt angles represent average values over macroscopic area of the SAM and thus can be taken as a fingerprint of the orientational order. Indeed, a totally disordered molecular film exhibits no linear dichroism and can be associated with an average tilt angle of a vector orbital of 54.7°, since $I(\alpha, \theta)$ does not depend on θ at $\alpha = 54.7^\circ$ [see Eq. (1)]. A deviation from this value, as seen for the SAMs studied here, means that a certain degree of orientational order exists, with a higher degree for a higher deviation. The highest orientational order is observed for the **BPT** and **5mBPT** SAMs, in accordance with the planar conformation of **5mBPT**^[44] and the assumed planar conformation of **BPT**,^[40,42a] such a conformation should favor high orientational order and dense molecular packing. Even slight deviation from the planar conformation, as is the case for **6mBPT**,^[45] results in a lower packing density (see previous section) and some deterioration of the orientational order (see Table 2). Finally,

Table 3. Molecular structure and charge transport properties of biphenylthiol SAMs.

	Molecular structure ^[a]	Torsion angle [°] ^[b]	n_{jn} ^[c]	J_{obs} ^[d]	J_{sc} ^[e]	Yield [%] ^[f]	$(\mu_{\log J } \pm \sigma)$ [A cm ⁻²] ^[g]	$\mu_J \times 10^{-3}$ [A cm ⁻²] ^[h]
5mBPT		1.1	24	8696	6	99.93	(-2.81 ± 0.62)	1.55
6mBPT		16.8	30	3292	18	99.45	(-2.30 ± 0.35)	5.01
BPT		36.4	20	3206	3	99.90	(-2.71 ± 0.10)	1.94
tBPT		79.7	34	6487	6	99.91	(-1.38 ± 0.58)	41.69

[a] Molecular structure of different **BPT** derivatives used. [b] Torsion angle between the planes of the phenyl rings from X-ray structure adapted from reference [23]. [c] Number of junctions formed. [d] Total number of J observations for each SAM. [e] Number of I - V traces that resulted in a short (i.e., junctions in which I reached 10^{-3} A). [f] Yield gives an estimate of work junctions, that is, the ratio of the difference between the total and shorting $J(V)$ traces to the total J observations. [g] Mean of $\log|J|$ from the log-normal distribution of J . [h] Mean value of J .

a distinct nonplanar conformation adopted by **tBPT** causes even lower packing density (see previous section) and even less orientational order (see Table 2). Thus, the results from the HRXPS and NEXAFS seem to corroborate the fact that the quality and packing density of the SAMs is the highest for the **BPT** SAM, slightly worse for the **5mBPT** SAMs, distinctly worse for the **6mBPT** SAMs, and the worst for the **tBPT** SAMs, in full correlation to the torsion angle in the biphenyl backbone. The slightly better quality of the **BPT** SAMs as compared to the **5mBPT** monolayers is presumably related to the presence of the side bridge in the last case, which can be associated with additional steric demands.

Electrical characterization: charge transport and OTFTs

Charge transport through biphenylthiol SAMs: To gain insight into the charge transport across the target SAMs supported on Au, we performed I - V measurements for two-terminal junctions by using a GaIn^E tip as the top counter electrode. We describe the junctions formed following the naming convention Au-SAM/Ga₂O₃|GaIn^E in which “-” indicates a covalently bonded contact, “/” denotes the physically formed contact between the surface of the SAM and the Ga₂O₃ layer, and “||” denotes the interface between Ga₂O₃ and GaIn^E bulk.

Tunneling is known to be the governing charge-transport mechanism through π -conjugated molecules shorter than about 3 nm.^[46] The current density (J) due to tunneling typically follows an exponential decay with molecular length according to the simplified approximation of Simmons model, $J = J_0 e^{-\beta d}$ in which d is the molecular length (in Å; in this present work d is considered to be the SAM effective thickness) and β (in Å⁻¹) is the tunneling decay constant. To gather an adequate amount statistical data for the range of charge tunneling through the target SAMs, we formed a minimum of at least 20 junctions for each of these monolayers and analyzed the resulting data without selecting or eliminating, any of the recorded data points to arrive at the

actual range of J distribution across each of the SAMs. The oxide skin covering the GaIn^E bulk was reported to have an electrical resistivity of 0.4 MΩ cm, corresponding to a J of 5.5 A cm⁻² at 0.2 V,^[4] which is much lower than the resistivity of any SAM in this study. The above current density is nearly three orders of magnitude greater than the analogous value for the **tBPT** SAM ($J = 2.1 \times 10^{-2}$ A cm⁻² at 0.2 V), which is the most conductive sample in this study. This would imply that the corresponding resistance of the least resistive **tBPT** SAM is about three orders of magnitude greater than the Ga₂O₃ layer. Hence, the resistivity contribution of the oxide skin to the overall J measured for the junctions can be reasonably neglected, since the total resistance is the direct sum of the two individual resistive components of the oxide in series with that of the SAM. Figure 3a shows the variation of the mean of $\log|J|$ with the applied bias across the junctions for all SAMs of this study. The charge transport through these monolayers clearly shows a trend that would be expected in the case of non-resonant tunneling.^[47] The distribution of J through the SAM follows a log-normal tendency this is attributed to the exponential dependence of charge tunneling over the distance d .^[9b,16c,48] Figure 3b displays the $\log|J|$ distributions for the **5mBPT**, **6mBPT**, **BPT** and **tBPT** SAMs. The log-normal histograms for each of the monolayers were populated by taking the $\log|J|$ values at a bias voltage of -0.4 V. From the peak of the Gaussian fitting of the histograms, it was possible to estimate the $\mu_{\log|J|}$ value, which offers an estimate of highest likelihood occurrence of J for a particular SAM. All histogram plotting and corresponding data analysis were done using the ggplot2^[49] package of R.^[50] Although in a chemisorbed SAM the molecules are believed to be arranged in well-ordered (i.e., similar to a 2D crystal pattern) manner, it is likely that there can be structural defects which may arise from several factors, including the presence of physisorbed adlayers, trace impurities on the electrode, and defects induced by the substrate surface profile among others. As these features influence the charge transport across the SAMs, it is imperative to acquire a large number data to

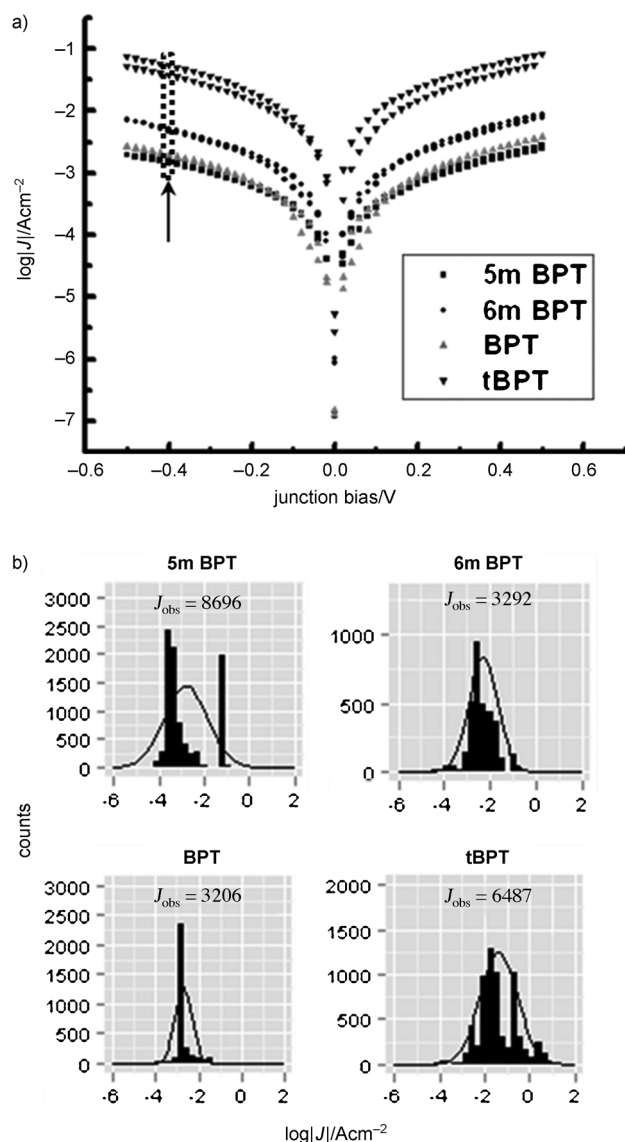


Figure 3. a) Characteristics of mean log current density as a function of junction bias for the Au-5m BPT/Ga₂O₃||GaIn^E, Au-6m BPT/Ga₂O₃||GaIn^E, Au-BPT/Ga₂O₃||GaIn^E and Au-tBPT/Ga₂O₃||GaIn^E junctions indicating forward and reverse traces. The arrow indicates the bias value from which the $\log|J|$ values were extracted to populate the histogram. b) $\log|J|$ distribution profiles at a bias of -0.4 V for the corresponding biphenylthiol SAMs 5m BPT, 6m BPT, BPT, and tBPT. The total number of recorded J observations (J_{obs}) are indicated in each histogram.

obtain a meaningful estimate of J for each of the target monolayers. In total more than 20000 J values were collected with a minimum of 3206 I - V traces recorded for each of the SAMs on at least two samples per SAM. The corresponding J values were used to populate the histograms. The statistical data for the recorded J values are collected in Table 3 along with the molecular chemical structure.

The higher degree of disorder and lower packing density of the tBPT SAMs influences the J showing clearly several distinct multiple peaks (with broader distribution range) in the $\log|J|$ histogram (see Figure 3b). This is in contrast with

the more narrow distribution of the $\log|J|$ in SAMs of BPT and 6m BPT, in which the molecules exhibit more order and a greater packing density on the electrode surface. The thickness of the SAMs depends on the tilt angle with respect to the surface normal, that is, the greater the tilt angle the lower the effective thickness that corresponds to the separation between electrodes. From the plot of $\log|J|$ versus d (i.e., effective monolayer thickness) the parameters J_0 and β can be extracted on the basis of the y-intercept and slope of the linear fit, respectively. We observed that the SAM with a greater tilt angle, that is, tBPT-SAM, was more conductive than that with a lower tilt angle, that is, 5m BPT-SAM, by a factor of about 27 in the linear scale (ca. 2 in $\log|J|$ magnitude). In oligo-aromatic architectures the charge-tunneling contributions probably result from through-bond and through-space tunneling.^[51] Owing to the minimal difference in the molecular length for the biphenylthiol derivatives, it was not possible to unequivocally resolve the influence of tunneling due to the through-bond molecular length. To understand if the current density exhibits dependence on the SAM medium, we plotted the $\log|J|$ with respect to the effective monolayer thickness (Figure 4). We observed a β of $(0.27 \pm 0.08) \text{ \AA}^{-1}$ from data extracted at a bias of -0.4 V (Figure 4); this is in agreement

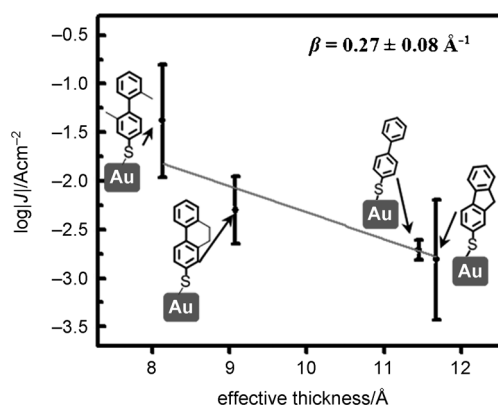


Figure 4. Plot of $\log|J|$ vs effective monolayer thickness for BPT SAMs at a bias of -0.4 V showing the respective tunneling decay factor estimated from the slope.

with the β extracted from a series of phenylene-oligomer-based SAMs measured in a large-area molecular junction.^[47b] On closer inspection of the decay of current density with respect to the effective thickness for the biphenylthiol monolayers, it is clear that there is characteristic attenuation with increase in the distance of separation. It is interesting to note that the $\log|J|$ dependence with cosine square torsion angle for our biphenylthiol SAMs exhibits an opposite trend observed in similar molecules on a single-molecule scale (see the Supporting Information).^[23] We attribute this to the likely weaker cohesive interaction between the SAM and top GaIn^E electrode,^[4] which is considered to be of van der Waals nature, being in contrast to the much stronger covalent

lent electronic coupling between the biphenyl dithiol molecules and gold electrodes studied by Vonlanthen et al.^[23]

Electrical characterization of OTFTs with biphenylthiol-SAM functionalized electrodes: To obtain information on the charge-injection properties of OTFT electrodes modified with biphenylthiol-based SAMs, we fabricated and characterized transistors in bottom-gate bottom-contact device geometry by using P3HT as active semiconducting layer. The channel length (L) and width (W) for the OTFTs under study amounted to 10 and 10000 μm , respectively. Given that the performance of OTFTs was sensitive enough to detect the subtle differences in charge-transport across SAMs chemisorbed on the source and drain electrodes,^[6a] we sought to determine the influence of the varying torsion-angle in the molecules composing the SAM.

The route to modify the electrode work function (Φ_{M}) by means of SAMs and thereby to adjust the energy levels in the system to either inject or extract charge carriers (electrons or holes) more effectively in organic electronic devices have been vastly exploited.^[7a,52] In particular, the chemisorption of alkanethiols and perfluoroalkanethiols has been used to lower or raise the work function of Au electrodes, respectively, to ultimately improve the injection of electron or holes.^[52a] The shift in the work function is generally attributed to the total of effective dipole moment formed between the Au–S bond along with the dipole moment due to the chemical composition of the molecule in the SAM,^[53] the tail groups contributing notably to the overall interfacial dipole.^[54] Among different possibilities, the work function of the metal can be measured by means of the contact potential difference (CPD) technique of a macroscopic Kelvin probe. We extracted the work function of Au electrodes coated with biphenyl-based SAMs from the CPD by using an Au reference tip ($\Phi \approx 5.1$ eV). Table 4 gives the respective data along with the work function of a bare Au electrode. The work function for the **BPT** SAM was measured to be about (4.81 ± 0.01) eV, which is in the range of the reported value in literature.^[7a] The work function difference between the more disordered Au-**tBPT** SAM with respect to the ordered Au-**BPT** SAM was approximately 210 meV, note that as the molecules are intrinsically quite non-polar, the effective shift in the work function due to the variability in packing densities and tilt angle of the assembled monolayer is fairly evident from the recorded values of Φ_{M} . The

surface wetting properties of the Au–SAM were estimated over macroscopic areas from static-water contact-angle (θ_{ca}) measurements giving values spanning between about 70 and 79° (see Table 4), highlighting a higher hydrophobic nature of the coated electrodes with respect to the bare gold. The θ_{ca} for Au-**BPT** SAM (ca. 78.9°) was in excellent agreement for a similar type of metal–SAM surface reported by us earlier.^[7a] Note that these values match closely to the contact angle reported in the literature for non-substituted biphenylthiol SAMs on Au(111).^[55]

The output (drain current (I_{D}) vs. source-drain voltage (V_{DS})) and transfer (I_{D} vs. gate voltage (V_{GS})) characteristics were measured for the devices incorporating electrodes modified with the **BPT** family of SAMs and compared with devices with non-functionalized electrodes. Figure 5 shows the OTFT device configuration and the I_{D} vs. V_{DS} plots obtained for the device with the **BPT**-SAM-modified electrodes. The recorded I_{D} vs. V_{GS} curves for the TFTs with the electrodes modified with the different SAMs are shown in Figure 6. The other key device performance indicators like

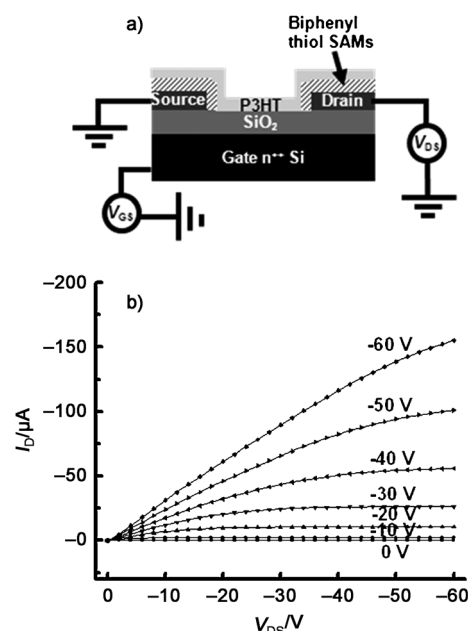


Figure 5. a) OTFT device geometry with biasing configurations. b) Output characteristics for TFT based on Au-**BPT** SAM modified electrodes ($W = 10000$ μm and $L = 10$ μm) with respective V_{GS} denoted.

Table 4. Contact angle, work function of electrodes, and other key device performance indicators.

Electrode surface	$(\theta_{\text{ca}} \pm \sigma)$ [°]	$(\Phi_{\text{M}} \pm \sigma)$ [eV]	$\Phi_{\text{bh+}}$ [meV] ^[a]	$(\mu_{\text{h+sat}} \pm \sigma) \times 10^{-3}$ [cm ² V ⁻¹ s ⁻¹] ^[b]	$(V_{\text{on}} \pm \sigma)$ [V]	$(V_{\text{T}} \pm \sigma)$ [V]
bare Au	(18.6 ± 4.2)	(4.88 ± 0.06)	25	(7.8 ± 1.0)	(8.8 ± 1.1)	(3.6 ± 0.6)
5mBPT	(71.6 ± 3.4)	(4.98 ± 0.02)	121	(6.7 ± 0.8)	(3.0 ± 5.4)	(-9.2 ± 5.5)
6mBPT	(69.3 ± 0.6)	(4.93 ± 0.02)	72	(7.2 ± 0.6)	(11.5 ± 1.4)	(0.3 ± 1.3)
BPT	(78.9 ± 1.9)	(4.81 ± 0.02)	43	(9.0 ± 0.6)	(5.5 ± 0.9)	(-8.4 ± 1.0)
tBPT	(68.0 ± 2.2)	(5.02 ± 0.03)	164	(6.4 ± 1.0)	(11.8 ± 1.9)	(2.2 ± 1.0)

[a] Hole injection barrier with respect to the IE level of P3HT. [b] Average hole mobility calculated in the saturation regime along with the standard deviation for at least 8 devices. The surface of the clean bare Au is hydrophilic,^[59] the θ_{ca} of which was measured within 60 s after performing UV/Ozone treatment.

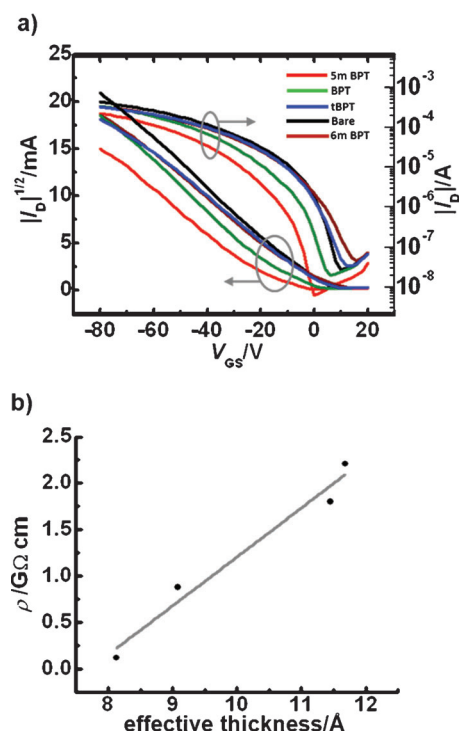


Figure 6. a) Transfer curves for the OTFTs based on electrodes with different **BPT** SAMs showing variation of square root of I_D vs V_{GS} (left axis) and semilog I_D vs V_{GS} (right axis) when $V_{DS} = -60$ V with lines indicating **5mBPT** (red), **6mBPT** (brown), **BPT** (green), **tBPT** (blue) and bare Au (black). b) Electrical resistivity dependence on effective thickness of the biphenylthiol SAMs estimated for a bias of -0.4 V with a linear least-squares fitting.

turn on voltage (V_{on}) and the threshold voltage (V_T) were estimated from the transfer plots. The V_{on} is the voltage value for which a change in slope sign occurs in the log scale on the transfer curves and was extracted from the I_D – V_{GS} in the linear regime. V_T is the intercept with the gate voltage axis from the plot of $\sqrt{|I_D|}$ versus V_{GS} (Figure 6) and provides the value of gate potential at which most of the traps levels are filled up. The hole injection barrier (Φ_{bh+}) is defined as the energy difference between ionization energy (IE) and the work function of the functionalized Au electrode. Note that the IE for the P3HT film used in our devices is about (4.86 ± 0.02) eV as measured by ambient photoelectron spectroscopy (see the Supporting Information). The evaluated injection barrier can give a good indication of the energetic mismatch at the metal–SAM/semiconductor interface. The field-effect mobility was extracted from the saturation regime by estimating the slope of $\sqrt{|I_D|}$ versus V_{GS} and then using Equation (3) in which C_i is the capacitance of the gate dielectric layer (230 nm of SiO_2) and has a value of 15 nF cm^{-2} .

$$\mu_{\text{sat}} = \frac{2L}{WC_i} \left(\frac{\partial \sqrt{|I_D|}}{\partial V_{GS}} \right)_{V_{DS}}^2 \quad (3)$$

For the P3HT solution, we used toluene, which has a high

boiling point (110.6°C), since it was reported that higher boiling point solvents tend to promote formation of polymeric micro crystalline domains in the active channel, which can enhance charge transport.^[56] The devices incorporating the **BPT** SAM exhibited the highest field-effect mobility with μ_{h+} of $9.0 \times 10^{-3} \text{ cm}^2 \text{ V}^{-1} \text{ s}^{-1}$. This result can be attributed to the combination of low energetic injection barrier and better electrode wettability by the nonpolar P3HT (the P3HT film has a θ_{ca} of ca. 106° on the surface of SiO_2)^[57] over the other, more hydrophobic **BPT**-based monolayer (see Table 4). The interfacial packing of the P3HT is likely to be better in more hydrophobic electrodes. In contrast, the devices with Au–**tBPT** electrodes exhibited the lowest field-effect mobility (μ_{h+} of $6.4 \times 10^{-3} \text{ cm}^2 \text{ V}^{-1} \text{ s}^{-1}$) in comparison with all other SAMs. This lower mobility for devices that contain Au–**tBPT** can be correlated with the relatively large hole injection barrier of 164 meV, which is greater by a factor of about 4 than the devices with highest mobility injection barrier for Au–**BPT** electrodes. The carrier mobility in organic semiconductors has been shown to be influenced by the injection barrier with the charge-injecting electrode.^[37] Hence, the lower the injection barrier, the higher is the current-injection efficiency. It has been shown for OTFTs that the contact resistance plays a big role in the lower source-drain bias,^[58] while at sufficiently high source-drain potentials the resistance offered by the contacts is limited.^[58b] Since we estimate the field-effect hole mobility at a V_{DS} of -60 V, the effect of the contact resistance has been reasonably omitted. Note that the standard deviation of mobility was within 15 % indicating good consistency for all the tested devices.

Discussion

In order to address the charge transport through the SAMs, the molecular structure, monolayer structural defects and packing density are among the pertinent factors that should be considered. The HRXPS data showed that the well-ordered **BPT** SAM on Au had a packing density about 1.5 times greater than the **tBPT** monolayer, which features the lowest orientational order. The molecular packing densities are probably heavily influenced by the intramolecular steric hindrance in **tBPT** SAM, which indeed features the highest torsion angle. Closer inspection of the histograms obtained from the charge-transport measurements revealed a narrower $\log|J|$ distribution for well-ordered **BPT**, **6m** and **5mBPT** SAMs if compared to the wider distribution for disordered **tBPT** SAM. This suggests that the measured J values are sensitive to the structural characteristics of the biphenyl SAMs chemisorbed on Au. We believe that the charge transport through our biphenylthiol SAMs is due to a combination of pathways tunneling through the molecule along with transport through interchain hops between adjacent molecules. While the length of the pathway through the molecular chain is the length of the molecule in its long axis, in the case of the parallel pathways model proposed by Slowin-

ski et al.^[51] the pathway due to through-space hops decreases with the effective thickness of the SAM. Least-squares fitting of the current density with the effective monolayer thickness yielded β of $(0.27 \pm 0.08) \text{ \AA}^{-1}$.

The electrical resistivity (ρ) of the biphenylthiol SAMs can be estimated from the current density (estimated from the charge transport measurements with GaIn^{E} probe) dependence with the applied electric field (E). As expected the ρ shows a monotonic increase with increasing effective thickness (Figure 6b). Note that despite the polycrystalline nature of the Au electrodes in the OTFT and the monocrystalline character of the Au used for the measurements with a GaIn^{E} -based junction (see Supporting Information for AFM images), a fairly good correlation between the electrical resistivity and the relative threshold voltage shift for the transistor comprising of biphenylthiol-coated electrodes was found. The V_{T} extracted from the transfer curve in Figure 6a was measured under biasing conditions in which V_{GS} was swept from $+20 \rightarrow -60$ V, while holding V_{DS} fixed at -60 V. It was observed that the V_{T} was about $+2.2$ V for transistors containing Au-**tBPT** SAM electrodes and the corresponding electrical resistivity $\rho \approx 0.12 \text{ G}\Omega\text{cm}$ also being the lowest; on the other hand, the devices with Au-**5mBPT** electrodes had a more negative shift of V_{T} of -9.2 V and the highest $\rho \approx 2.2 \text{ G}\Omega\text{cm}$ (see Figure 6b). This difference in the V_{T} for devices based on Au-**5mBPT** electrodes of nearly 18 V in the upper bounds when compared Au-**tBPT** can be attributed directly to the resistivity increase by a similar one-to-one correlation (i.e., the ρ increases by factor of about 18 for electrodes containing **5mBPT** with respect to **tBPT** SAMs). For P3HT transistors the majority charge carrier are holes (i.e., increase in I_{D} tends to predominantly occur when V_{GS} is negative). Note that while the potential sweep for the gate electrode starts from positive voltage and proceeds to the negative (Figure 6a) the TFTs exhibited V_{T} shifts towards more negative voltages in the order of **tBPT**, **6mBPT**, **BP**, and **5mBPT**, being in good agreement with the concomitant trend of increasing resistivity through the biphenylthiol SAMs. The OTFT charge-carrier mobility unambiguously reveals, as expected, that the hole injection barrier from the electrodes plays an important role in the transport through the semiconducting film (Figure 7). It is interesting to note that although the injection barrier for bare Au and Au-**BPT** electrodes were in the same range, confined within error bars (see Table 4), for the device with just the bare gold the mobility was about $0.0078 \text{ cm}^2\text{V}^{-1}\text{s}^{-1}$, which in comparison to devices with Au-**BPT** electrodes were lower by a factor of about 1.2.

The top-surface morphology of the P3HT film on the modified electrodes exhibited an isotropic grain-like pattern (see the respective AFM images in the Supporting Information) featuring a fairly similar root-mean-square roughness (R_{RMS}). The increase in mobility for devices with **BPT**-coated electrodes can be attributed to the better arrangement of the semiconductor at the interface with the more hydrophobic surface over the bare hydrophilic Au electrode surface, which having a similar injection barrier has a lower

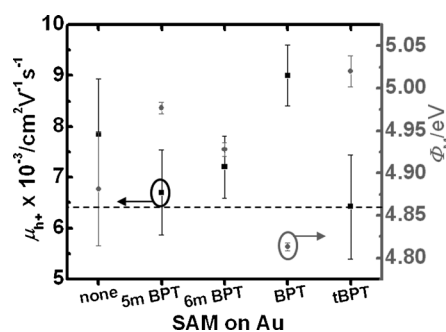


Figure 7. Hole carrier mobility in saturation mode and respective work function for OTFTs based on electrodes with and without biphenylthiol SAMs. The dashed line indicates the ionization energy level of P3HT, which is taken as the reference to estimate the hole injection/extraction barrier to the source-drain electrode.

mobility than the Au-**BPT** which has a more hydrophobic surface. This suggests that, as in various cases previously reported in literature, the mobility of our TFTs is dictated by 1) the injection barrier of electrode with semiconductor, 2) electrode surface wettability of the semiconductor film and also 3) the packing density of the molecules in the SAM. The well-ordered **BPT** SAM on electrodes exhibited a mobility which was about 1.4 times greater than that of the mobility for devices based on more disordered Au-**tBPT** SAM, indeed reflecting the variable packing density of the molecules adsorbed on the Au electrodes and the energetic mismatch at the metal-SAM/semiconductor interface. Overall, the transistor responses show that our devices are an effective means to monitor the energy-level adjustment and the corresponding electronic coupling at the interface and the threshold voltage-shift scale with the tunneling resistivity through the biphenyl SAMs on the Au electrodes.

Conclusion

In summary, the charge transport through a family of biphenylthiol-based SAMs with varying torsion angles chemisorbed on Au surfaces exhibits a good degree of correlation with the packing density and orientational order in the monolayers. The last parameters were mostly governed by molecular conformation, which was specifically adjusted by the site bridging or substitution of/at the individual phenyl rings. The efficiency of the charge tunneling through the SAMs shows a characteristic decay with the increasing separation between the metallic contacts (i.e., increase of the effective SAM thickness). The charge-transport experiments revealed a through-space β of $(0.27 \pm 0.08) \text{ \AA}^{-1}$. For transistors the shift in the threshold voltage scaled as a function of resistivity through the biphenyl SAMs on the electrodes. A good agreement between the transistor-electrode/SAM energetic-injection-barrier dependence on the field-effect mobility was found. These results show that a proper design of thiolated molecules chemisorbed on Au electrodes is needed

for realizing more efficient organic electronic devices through improved control over the electrode–semiconductor interface.

Acknowledgements

This work was supported by the ERC project SUPRAFUNCTION (GA-257305), the International Center for Frontier Research in Chemistry (icFRC, Strasbourg), and the German Research Foundation (DFG) through the grant ZH 63/14-1. N.C. thanks the Marie-Curie IEF-OPTSU-FET (PIEF-GA-2009-235967), while E.O. and A. M.M. acknowledge the ITN-SUPERIOR (PITN-GA-2009-238177) for their fellowships. Research in Basel was supported by the Swiss National Science Foundation (SNF) and the Swiss Nanoscience Institute (SNI). R.T. and M.Z. thank A. Nefedov and C. Wöll (KIT) for the technical cooperation at BESSY II as well as BESSY II staff for the assistance during the synchrotron-based experiments.


- [1] A. Aviram, M. A. Ratner, *Chem. Phys. Lett.* **1974**, *29*, 277–283.
- [2] a) L. Venkataraman, J. E. Klare, C. Nuckolls, M. S. Hybertsen, M. L. Steigerwald, *Nature* **2006**, *442*, 904–907; b) J. M. Mativetsky, G. Pace, M. Elbing, M. A. Rampi, M. Mayor, P. Samorì, *J. Am. Chem. Soc.* **2008**, *130*, 9192–9193; c) C. A. Nijhuis, W. F. Reus, A. C. Siegel, G. M. Whitesides, *J. Am. Chem. Soc.* **2011**, *133*, 15397–15411.
- [3] a) C. D. Bain, G. M. Whitesides, *Science* **1988**, *240*, 62; b) W. B. Caldwell, D. J. Campbell, K. Chen, B. R. Herr, C. A. Mirkin, A. Malik, M. K. Durbin, P. Dutta, K. G. Huang, *J. Am. Chem. Soc.* **1995**, *117*, 6071–6082; c) G. Pace, V. Ferri, C. Grave, M. Elbing, C. von Hänisch, M. Zharnikov, M. Mayor, M. A. Rampi, P. Samorì, *Proc. Natl. Acad. Sci. USA* **2007**, *104*, 9937–9942.
- [4] C. A. Nijhuis, W. F. Reus, G. M. Whitesides, *J. Am. Chem. Soc.* **2009**, *131*, 17814–17827.
- [5] a) N. Crivillers, E. Orgiu, F. Reinders, M. Mayor, P. Samorì, *Adv. Mater.* **2011**, *23*, 1447–1452; b) S. Karpe, M. Ocafrain, K. Smaali, S. Lenfant, D. Vuillaume, P. Blanchard, J. Roncali, *Chem. Commun.* **2010**, *46*, 3657–3659; c) A. J. Kronemeijer, H. B. Akkerman, T. Kudernac, B. J. van Wees, B. L. Feringa, P. W. M. Blom, B. de Boer, *Adv. Mater.* **2008**, *20*, 1467–1473.
- [6] a) P. Stoliar, R. Kshirsagar, M. Massi, P. Annibale, C. Albonetti, D. M. De Leeuw, F. Biscarini, *J. Am. Chem. Soc.* **2007**, *129*, 6477–6484; b) X. Cheng, Y. Y. Noh, J. Wang, M. Tello, J. Frisch, R. P. Blum, A. Vollmer, J. P. Rabe, N. Koch, H. Sirringhaus, *Adv. Funct. Mater.* **2009**, *19*, 2407–2415.
- [7] a) E. Orgiu, N. Crivillers, J. Rotzler, M. Mayor, P. Samorì, *J. Mater. Chem.* **2010**, *20*, 10798; b) M. E. Gemayel, M. Treier, C. Musumeci, C. Li, K. Müllen, P. Samorì, *J. Am. Chem. Soc.* **2012**, *134*, 2429–2433.
- [8] a) V. B. Engelkes, J. M. Beebe, C. D. Frisbie, *J. Am. Chem. Soc.* **2004**, *126*, 14287–14296; b) V. B. Engelkes, J. M. Beebe, C. D. Frisbie, *J. Phys. Chem. B* **2005**, *109*, 16801–16810.
- [9] a) Y. Selzer, A. Salomon, D. Cahen, *J. Phys. Chem. B* **2002**, *106*, 10432–10439; b) E. A. Weiss, R. C. Chiechi, G. K. Kaufman, J. K. Kriebel, Z. Li, M. Duati, M. A. Rampi, G. M. Whitesides, *J. Am. Chem. Soc.* **2007**, *129*, 4336–4349.
- [10] a) M. T. González, S. M. Wu, R. Huber, S. J. van der Molen, C. Schonenberger, M. Calame, *Nano Lett.* **2006**, *6*, 2238–2242; b) M. A. Reed, C. Zhou, C. J. Muller, T. P. Burgin, J. M. Tour, *Science* **1997**, *278*, 252–254; c) J. Reichert, R. Ochs, D. Beckmann, H. B. Weber, M. Mayor, H. von Lohneysen, *Phys. Rev. Lett.* **2002**, *88*, 176804.
- [11] X. D. Cui, A. Primak, X. Zarate, J. Tomfohr, O. F. Sankey, A. L. Moore, T. A. Moore, D. Gust, G. Harris, S. M. Lindsay, *Science* **2001**, *294*, 571–574.
- [12] W. Wang, T. Lee, M. A. Reed, *Phys. Rev. B* **2003**, *68*, 035416.
- [13] J. G. Kushmerick, D. B. Holt, J. C. Yang, J. Naciri, M. H. Moore, R. Shashidhar, *Phys. Rev. Lett.* **2002**, *89*, 086802.
- [14] A. P. Bonifas, R. L. McCreery, *Nat. Nanotechnol.* **2010**, *5*, 612–617.
- [15] R. C. Chiechi, E. A. Weiss, M. D. Dickey, G. M. Whitesides, *Angew. Chem.* **2008**, *120*, 148–150; *Angew. Chem. Int. Ed.* **2008**, *47*, 142–144.
- [16] a) D. Fracasso, H. Valkenier, J. C. Hummelen, G. C. Solomon, R. C. Chiechi, *J. Am. Chem. Soc.* **2011**, *133*, 9556–9563; b) G. D. Lilly, A. C. Whalley, S. Grunder, C. Valente, M. T. Frederick, J. F. Stoddart, E. A. Weiss, *J. Mater. Chem.* **2011**, *21*, 11492–11497; c) M. M. Thuo, W. F. Reus, C. A. Nijhuis, J. R. Barber, C. Kim, M. D. Schulz, G. M. Whitesides, *J. Am. Chem. Soc.* **2011**, *133*, 2962–2975.
- [17] Yield is referred to as the ratio of the difference between the total number of $J(V)$ traces to the traces that ended up with a short (instrument reached compliance limit) with the total J observations.
- [18] a) E. Tran, M. Duati, V. Ferri, K. Müllen, M. Zharnikov, G. M. Whitesides, M. A. Rampi, *Adv. Mater.* **2006**, *18*, 1323–1328; b) V. Ferri, M. Elbing, G. Pace, M. D. Dickey, M. Zharnikov, P. Samorì, M. Mayor, M. A. Rampi, *Angew. Chem.* **2008**, *120*, 3455–3457; *Angew. Chem. Int. Ed.* **2008**, *47*, 3407–3409.
- [19] H. B. Akkerman, P. W. M. Blom, D. M. de Leeuw, B. de Boer, *Nature* **2006**, *441*, 69–72.
- [20] G. Wang, Y. Kim, M. Choe, T.-W. Kim, T. Lee, *Adv. Mater.* **2011**, *23*, 755–760.
- [21] a) J. C. Love, L. A. Estroff, J. K. Kriebel, R. G. Nuzzo, G. M. Whitesides, *Chem. Rev.* **2005**, *105*, 1103–1170; b) Y. Qi, I. Ratera, J. Y. Park, P. D. Ashby, S. Y. Quek, J. B. Neaton, M. Salmeron, *Langmuir* **2008**, *24*, 2219–2223.
- [22] a) D. Li, B. I. Swanson, J. M. Robinson, M. A. Hoffbauer, *J. Am. Chem. Soc.* **1993**, *115*, 6975–6980; b) F. Anariba, J. K. Steach, R. L. McCreery, *J. Phys. Chem. B* **2005**, *109*, 11163–11172; c) W. Haiss, C. Wang, R. Jitchati, I. Grace, S. Martín, A. S. Batsanov, S. J. Higgins, M. R. Bryce, C. J. Lambert, P. S. Jensen, R. J. Nichols, *J. Phys. Condens. Matter* **2008**, *20*, 374119; d) A. B. Ricks, G. C. Solomon, M. T. Colvin, A. M. Scott, K. Chen, M. A. Ratner, M. R. Wasielewski, *J. Am. Chem. Soc.* **2010**, *132*, 15427–15434; e) G. Bruno, F. Babudri, A. Operamolla, G. V. Bianco, M. Losurdo, M. M. Giangregorio, O. H. Omar, F. Mavelli, G. M. Farinola, P. Capezzuto, F. Naso, *Langmuir* **2010**, *26*, 8430–8440; f) A. Operamolla, O. H. Omar, F. Babudri, G. M. Farinola, F. Naso, *J. Org. Chem.* **2007**, *72*, 10272–10275; g) S. Casalini, F. Leonardi, C. A. Bortolotti, A. Operamolla, O. Hassan, L. Paltrinieri, C. Albonetti, G. M. Farinola, F. Biscarini, *J. Mater. Chem.* **2012**, *22*, 12155–12163.
- [23] a) A. Mishchenko, D. Vonlanthen, V. Meded, M. Bürkle, C. Li, I. V. Pobelov, A. Bagrets, J. K. Viljas, F. Pauly, F. Evers, M. Mayor, T. Wandlowski, *Nano Lett.* **2010**, *10*, 156–163; b) D. Vonlanthen, A. Mishchenko, M. Elbing, M. Neuburger, T. Wandlowski, M. Mayor, *Angew. Chem.* **2009**, *121*, 9048–9052; *Angew. Chem. Int. Ed.* **2009**, *48*, 8886–8890.
- [24] A. Mishchenko, L. A. Zotti, D. Vonlanthen, M. Bürkle, F. Pauly, J. C. Cuevas, M. Mayor, T. Wandlowski, *J. Am. Chem. Soc.* **2011**, *133*, 184–187.
- [25] S. Woitellier, J. Launay, C. Joachim, *Chem. Phys.* **1989**, *131*, 481–488.
- [26] a) B. Jäger, H. Schürmann, H. U. Müller, H. J. Himmel, M. Neumann, M. Grunze, C. Wöll, *Z. Phys. Chem.* **1997**, *202*, 263–272; b) M. Wirde, U. Gelius, T. Dunbar, D. L. Allara, *Nucl. Instrum. Methods Phys. Res. Sect. B* **1997**, *131*, 245–251; c) M. Zharnikov, M. Grunze, *J. Vac. Sci. Technol. B* **2002**, *20*, 1793–1807.
- [27] X-ray photoelectron spectrometers—calibration of the energy scales, ISO 15472 Surface chemical analysis **2001**.
- [28] W. Azzam, B. I. Wehner, R. A. Fischer, A. Terfort, C. Wöll, *Langmuir* **2002**, *18*, 7766–7769.
- [29] J. Stöhr, *NEXAFS spectroscopy*, Springer, Berlin, New York, **1992**.
- [30] S. Frey, V. Stadler, K. Heister, W. Eck, M. Zharnikov, M. Grunze, B. Zeysing, A. Terfort, *Langmuir* **2001**, *17*, 2408–2415.
- [31] P. E. Batson, *Phys. Rev. B* **1993**, *48*, 2608–2610.
- [32] R. S. Timsit, *Appl. Phys. Lett.* **1982**, *40*, 379–381.
- [33] A. Shaporenko, M. Elbing, A. Blaszczyk, C. von Hänisch, M. Mayor, M. Zharnikov, *J. Phys. Chem. B* **2006**, *110*, 4307–4317.
- [34] M. Zharnikov, M. Grunze, *J. Phys. Condens. Matter* **2001**, *13*, 11333.

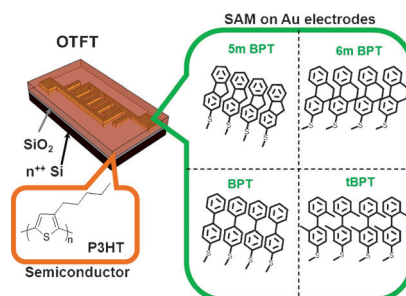
- [35] M. Zharnikov, *J. Electron Spectrosc. Relat. Phenom.* **2010**, *178*, 380–393.
- [36] J. A. Horsley, J. Stohr, A. P. Hitchcock, D. C. Newbury, A. L. Johnson, F. Sette, *J. Chem. Phys.* **1985**, *83*, 6099–6107.
- [37] Y. Shen, M. W. Klein, D. B. Jacobs, J. Campbell Scott, G. G. Malliaras, *Phys. Rev. Lett.* **2001**, *86*, 3867–3870.
- [38] C. Fuxen, W. Azzam, R. Arnold, G. Witte, A. Terfort, C. Wöll, *Langmuir* **2001**, *17*, 3689–3695.
- [39] T. Yokoyama, K. Seki, I. Morisada, K. Edamatsu, T. Ohta, *Phys. Scr.* **1990**, *41*, 189.
- [40] A. Hargreaves, S. H. Rizvi, *Acta Crystallogr.* **1962**, *15*, 365–373.
- [41] N. Ballav, B. Schüpbach, O. Dethloff, P. Feulner, A. Terfort, M. Zharnikov, *J. Am. Chem. Soc.* **2007**, *129*, 15416–15417.
- [42] a) J. Trotter, *Acta Crystallogr.* **1961**, *14*, 1135–1140; b) A. Bashir, D. Käfer, J. Müller, C. Wöll, A. Terfort, G. Witte, *Angew. Chem.* **2008**, *120*, 5328–5331; *Angew. Chem. Int. Ed.* **2008**, *47*, 5250–5252.
- [43] a) S. C. Chang, I. Chao, Y. T. Tao, *J. Am. Chem. Soc.* **1994**, *116*, 6792–6805; b) A. A. Dhirani, R. W. Zehner, R. P. Hsung, P. Guyot-Sionnest, L. R. Sita, *J. Am. Chem. Soc.* **1996**, *118*, 3319–3320.
- [44] G. M. Brown, M. H. Bortner, *Acta Crystallogr.* **1954**, *7*, 139.
- [45] R. Cosmo, T. W. Hambley, S. Sternhell, *J. Org. Chem.* **1987**, *52*, 3119–3123.
- [46] a) S. Ho Choi, B. Kim, C. D. Frisbie, *Science* **2008**, *320*, 1482–1486; b) Q. Lu, K. Liu, H. Zhang, Z. Du, X. Wang, F. Wang, *ACS Nano* **2009**, *3*, 3861–3868.
- [47] a) T. Ishida, W. Mizutani, Y. Aya, H. Ogiso, S. Sasaki, H. Tokumoto, *J. Phys. Chem. B* **2002**, *106*, 5886–5892; b) A. Kronemeijer, E. Huisman, H. Akkerman, A. Goossens, I. Katsouras, P. van Hal, T. Geuns, S. van der Molen, P. Blom, D. de Leeuw, *Appl. Phys. Lett.* **2010**, *97*, 173302.
- [48] C. A. Nijhuis, W. F. Reus, G. M. Whitesides, *J. Am. Chem. Soc.* **2010**, *132*, 18386–18401.
- [49] H. Wickham, *ggplot2: elegant graphics for data analysis*, Springer, New York **2009**.
- [50] R Development Core Team, *R: A language and environment for statistical computing*, Springer, Vienna, Austria **2011**.
- [51] K. Slowinski, R. V. Chamberlain, C. J. Miller, M. Majda, *J. Am. Chem. Soc.* **1997**, *119*, 11910–11919.
- [52] a) B. de Boer, A. Hadipour, M. M. Mandoc, T. van Woudenberg, P. W. M. Blom, *Adv. Mater.* **2005**, *17*, 621–625; b) G. Heimel, L. Romaner, E. Zojer, J. L. Bredas, *Acc. Chem. Res.* **2008**, *41*, 721–729; c) S. A. DiBenedetto, A. Facchetti, M. A. Ratner, T. J. Marks, *Adv. Mater.* **2009**, *21*, 1407–1433; d) D. Boudinet, M. Benwadih, Y. Qi, S. Altazin, J. M. Verilhac, M. Kroger, C. Serbutoviez, R. Gwoziecki, R. Coppard, G. Le Blevennec, *Org. Electron.* **2010**, *11*, 227–237; e) K. Singh, T. Nelson, J. Belot, T. Young, N. R. Dhumal, T. Kowalewski, R. McCullough, P. Nachimuthu, S. Thevuthasan, L. M. Porter, *ACS Appl. Mater. Interfaces* **2011**, *3*, 2973–2978.
- [53] G. Heimel, L. Romaner, E. Zojer, J.-L. Brédas, *Nano Lett.* **2007**, *7*, 932–940.
- [54] a) I. Campbell, S. Rubin, T. Zawodzinski, J. Kress, R. Martin, D. Smith, N. Barashkov, J. Ferraris, *Phys. Rev. B* **1996**, *54*, R14321–R14324; b) N. V. Venkataraman, S. Zürcher, A. Rossi, S. Lee, N. Naujoks, N. D. Spencer, *J. Phys. Chem. C* **2009**, *113*, 5620–5628.
- [55] J. F. Kang, A. Ulman, S. Liao, R. Jordan, G. H. Yang, G. Y. Liu, *Langmuir* **2001**, *17*, 95–106.
- [56] J. F. Chang, B. Sun, D. W. Breiby, M. M. Nielsen, T. I. Sölling, M. Giles, I. McCulloch, H. Sirringhaus, *Chem. Mater.* **2004**, *16*, 4772–4776.
- [57] L. Robinson, J. Isaksson, N. D. Robinson, M. Berggren, *Surfactant Sci. Ser.* **2006**, *600*, L148–L152.
- [58] a) G. Horowitz, R. Hajlaoui, R. Bourguiga, M. Hajlaoui, *Synth. Met.* **1999**, *101*, 401–404; b) V. Podzorov, S. E. Sysoev, E. Loginova, V. M. Pudalov, M. E. Gershenson, *Appl. Phys. Lett.* **2003**, *83*, 3504–3506.
- [59] C. G. Worley, R. W. Linton, *J. Vac. Sci. Technol. A* **1995**, *13*, 2281–2284.
- [60] S. Liao, R. Harvey, J. Pataki, EP0363128 (A2), **1990**.

Received: May 28, 2012
Published online: ■ ■ ■, 0000

Molecular Electronics

A. M. Masillamani, N. Crivillers,
E. Orgiu, J. Rotzler, D. Bossert,
R. Thippeswamy, M. Zharnikov,*
M. Mayor,* P. Samorì* ■■■■–■■■■

 **Multiscale Charge Injection and Transport Properties in Self-Assembled Monolayers of Biphenyl Thiols with Varying Torsion Angles**



Controlled charge injection! Biphenylthiols with different substituents between phenyl groups in the bridge position, once chemisorbed onto gold source-drain electrodes, can be used to vary the charge injection and electrical performances of organic thin-film transistors. By varying the torsion angle between the phenyl rings one can introduce changes in packing densities and tilt angles of the molecules self-assembled on the electrode that play a direct role influencing the charge transport through the molecular monolayer (see figure).